Applied Surface Science 476 (2019) 1000–1007

Contents lists available at ScienceDirect

Applied Surface Science

journal homepage: www.elsevier.com/locate/apsusc

Full length article

Controlling the phenolic resin-based amorphous carbon content for enhancing cycling stability of Si nanosheets@C anodes for lithium-ion batteries

Jingshuang Liang[a], Fengli Huo[a], Zhongyuan Zhang[a], Wenfei Yang[a], Muhammad Javid[a], Youngguan Jung[c], Xinglong Dong[a,*], Guozhong Cao[b]

[a] *Key Laboratory of Materials Modification by Laser, Ion and Electron Beams (Ministry of Education), School of Materials Science and Engineering, Dalian University of Technology, Dalian 116023, PR China*
[b] *Department of Materials Science and Engineering, University of Washington, Seattle, WA 98195, USA*
[c] *Department of Mechanical Engineering, Kumoh National Institute of Technology, Daeharkro 53, Gumi, Gyeong-Buk 730-701, South Korea*

ARTICLE INFO

Keywords:
Si nanosheets@C nanocomposite
Arc-discharge plasma
Phenolic resin
Lithium-ion battery
Anode

ABSTRACT

Carbon-coated Si nanosheets (Si NSs@C) nanocomposites with different carbon contents are successfully controlled and synthesized by the method of DC arc-discharge plasma, followed by phenolic resin pyrolysis at high temperature. The electrochemical performances of these nanocomposites as the anodes of lithium-ion batteries (LIBs) are investigated. The Si NSs with an average size of 31 nm and a thickness of 2.4 nm are surrounded by phenolic resin-derived amorphous carbon, forming a cladding structure. In the nanocomposites, Si NSs play a leading role in the reaction with Li^+ ions, while the amorphous carbon mainly provides a highly conductive matrix for good contact among Si NSs active phases, which further facilitates the diffusion and transport of Li^+ ions and electrons. The carbon matrix can also protect Si NSs from direct contact with the electrolyte, to ensure the formation of stable SEI films in cycles. Electrochemical performances indicate that the Si NSs@C nanocomposite electrode with the carbon content of 66.4 wt% delivers a stable discharge specific capacity of 822 mAh g^{-1} at a current density of 100 mA g^{-1} after 200 cycles and a better rate capability, confirming the predominant role of the controlled carbon content in the enhancement of the cycling stability of such Si-based anodes for LIBs.

1. Introduction

With the development of science and technology, as well as the continuous innovation of electronic products, the power supplies as the core component of electrical devices have become the focus of researches [1,2]. Among them, lithium-ion batteries (LIBs) with high energy density and good cycle performance have become power storage devices widely used in communications, aviation and military industry [3,4]. Graphite as the traditional anode material of LIBs fails to meet the increasing demands of energy storage markets due to its theoretical specific capacity limit of 372 mAh g^{-1} [5]. Therefore, it is the common aspiration of researchers to research and develop a new generation of anode materials with high specific capacity, long cycle life, low cost, extensive applicability and nontoxicity [6–9]. Silicon, the next-most abundant nontoxic element on the earth has received significant attention as an alternative anode material for next generation of LIBs [10,11]. It possesses the highest ever-known theoretical capacity of 4200 mAh g^{-1} and a low discharge potential of 370 mV (vs Li/Li^+), giving rise to a long plateau in the discharge curve [12]. However, Si-based anodes still face challenges including volume expansion by 300% caused by lithiation and delithation processes, which further leads to fracture and loss of electrical contact inside of active materials, unstable growth of solid electrolyte interface (SEI) films on the Si surface and ultimately rapid degradation of capacity [13]. Beyond that, Si is known as one kind of semiconductor materials with inferior electrical conductivity, contributing to low active material utilization and poor rate capability as electrodes. In view of the above-mentioned problems, it is crucial to find an appropriate method for enhancing the electrochemical properties and conductivity of Si anode materials. Recently, many researchers have turned to the design of nanoscale materials with different structures and morphologies including nanospheres, nanosheets, nanowires, thin films, porous structure and so on [14–18].

---

* Corresponding author.
E-mail address: dongxl@dlut.edu.cn (X. Dong).

https://doi.org/10.1016/j.apsusc.2019.01.220
Received 28 September 2018; Received in revised form 23 January 2019; Accepted 24 January 2019

This will effectively shorten the diffusion pathway of Li^+ ions, alleviate the strain caused by volume expansion and contraction, improve the capacity retention and prolong the cycle life compared with micro-sized Si particles. However, the conductivity still needs to be enhanced. And large specific surface area of nanoscale materials may reduce the interfacial stability. Therefore, it is inevitably necessary to combine nanoscale Si units with a second phase (e.g. carbon) as well as the subsequent assembly, so as to stabilize the solid electrolyte interphase (SEI) on the surface of individual Si, strengthen the interfacial electrical contacts between active units and enhance the conductivity [19]. With that in mind, Si/C nanocomposite has become a hot research topic because of its special physical and chemical properties. Dispersing Si in various types of ductile carbon matrix, such as carbon coating [20–24], carbon nanotubes [25], carbon nanofibers [26] and graphene [27], has been widely used as a support for Si particles to utilize their high electrical conductivity and tunable structures. The carbon matrix can not only provide continuous long-distance transport pathways for electrons, but also supply numerous active sites for charge transfer reactions. Furthermore, carbon matrix acts as a physical buffering layer buffering the large volume changes. Shen et al. designed pomegranate-structured Si/C composite spheres, delivering a superior cycling stability of 581 mAh g^{-1} at a current density of 0.2 A g^{-1} after 100 cycles and achieving a noticeable high-rate capacity of 421 mAh g^{-1} even at a high current density of 1 A g^{-1} [28]. Yue et al. prepared graphene-wrapped Si nanoparticles (NPs), exhibiting significantly improved lithium storage performance with a superior rate capability as well as a large reversible capacity of 1482 mAh g^{-1} at a current density of 210 mA g^{-1} after 300 cycles [24]. Liang et al. synthesized silicon-embedded porous carbon microsphere anode with an exceptional conductive framework for ions and electrons, exhibiting a high capacity of 1325 mAh g^{-1} at 0.2 A g^{-1} after 60 cycles as well as a superior rate capability with a capacity of 925 mAh g^{-1} at a large current density of 5 A g^{-1} [11]. All of these electrochemical performances are much better than those of the bare Si electrode.

Although the electrochemical performances of those works mentioned above have been greatly improved, complex experimental procedures and expensive nanoscale materials have immensely hindered their extensive production and application. From this point of view, it is necessary to explore some other easier cheaper, and more effective methods for designing and synthesizing the materials with nanoscale structures and morphologies. In the present paper, 2D Si nanosheets (NSs) as a Si source were synthesized using DC arc-discharge method under the mixed atmosphere of argon and hydrogen. As a traditional technique, this method is well known for high yield, high purity of nanopowder products and ease of fabricating particular kinds of nanostructures [29]. Due to its thermal stability, flame retardancy, char retention ability, and high mechanical strength, phenolic resin [30–32] is selected as the precursor of carbon to prepare Si NSs@C nanocomposites through high-temperature pyrolysis technique. This is favorable to the cycle stability of electrodes. However, the difference in carbon content among integral materials always leads to diverse capacity contributions. We controlled different ratios of phenolic resin to Si in the preparation process to optimize the compositions and structures, thus enhancing the cycling stability of nanocomposite electrodes. Si NSs were surrounded by amorphous carbon with different thicknesses, depending on the content of introduced phenolic resin. The electrochemical testing results show that the nanocomposite with carbon content of 66.4 wt% possesses relatively stable electrochemical performance as an anode material for LIBs.

2. Experimental

2.1. Synthesis of Si NSs@C nanocomposite powders

Two-dimensional Si NSs were synthesized by the method of DC arc-discharge plasma [15,29]. The bulk Si was served as a raw material and an anode of the arc-discharge plasma. Meanwhile, a tungsten rod was used as a cathode. The arc-discharge was operated under a mixed working atmosphere of inert argon and active hydrogen (Ar: 0.02 MPa, H_2: 0.01 MPa) after the working chamber was vacuumed. To ignite the arc, the distance between the bulk and the tungsten rod needed to be adjusted constantly to avoid the arc interruption caused by the consumption of Si bulk. Then the Si bulk was evaporated into Si NSs at a steady current of 90 A and a steady voltage of 20 V which were controlled by an electrical device. Prior to collection, 0.00125 MPa of air was imported into the chamber to passivate the fresh Si NSs. And they were collected together from the water-cooled chamber 12 h later.

Si NSs@C nanocomposite was synthesized using the following procedure. 1 g phenolic resin was dissolved in 20 ml ethyl alcohol under continuous ultrasonic stirring to make the phenolic resin dissolve rapidly. Next, 1 g Si NSs were added into the above solution to form sol under magnetic stirring for 2 h in a water bath. After magnetic stirring, the water bath temperature was raised to 60 °C, the ethyl alcohol was vaporized and the solution was turned into gel. Then, the gel was dried in a thermostat oven at a temperature of 60 °C for 12 h. After thoroughly drying, the dried gel was taken out and crushed in a mortar, and then transferred into an energy-saving program controlled vacuum furnace for pyrolysis at 600 °C under argon atmosphere for 2 h. Finally, the Si NSs@C nanocomposite was obtained after the temperature cooled down naturally to the ambient temperature. For optimizing the carbon content in the samples, 4 g and 5 g phenolic resins were separately combined with 1 g Si NSs to prepare another two samples by the same method. Si NSs@C nanocomposites using different contents of phenolic resin (1 g, 4 g and 5 g) were separately denoted as B_1, B_2 and B_3 in the paper.

2.2. Structural characterization of carbon, Si NSs and Si NSs@C nanocomposites

Crystal structures of carbon, Si NSs and Si NSs@C nanocomposites were characterized by X-ray diffraction (PANalytical Empyrean) using Cu K_α radiation ($\lambda = 1.5416$ Å) in the diffraction angle range of 20°–80°. Thermogravimetric analysis was carried out using a TGA/SDTA851 type instrument (Mettler Toledo, Switzerland) from the ambient temperature to 800 °C under flowing air at a heating rate of 10 °C min^{-1}. Microstructures and morphologies were investigated using transmission electron microscope (TEM, Tecnai220 S-TWIM). Carbon species were characterized by Raman spectroscope with the Red Light laser line at 532 nm (InVia).

2.3. Electrochemical measurements on Si NSs@C nanocomposites electrodes

Electrochemical tests were carried out upon Si NSs@C nanocomposites as working electrodes using CR2025 coin-type half cells assembled in an Ar-filled glove box (Etelux Lab 2000). Both contents of moisture and oxygen were less than 0.1 ppm. Lithium foils served as counter electrodes (Shanghai Shunyou Metal Material Co., Ltd). 1 M $LiPF_6$ dissolved in ethylene carbonate (EC) and diethyl carbonate (DEC) with a volume ratio of 1:1 (Beijing Chemical Reagent Research Institute) was used as the electrolyte. Meanwhile, a polypropylene (PP) film (Celgard 2400) was used as the separator. The working electrodes were prepared by mixing active Si NSs@C nanocomposite (70 wt%), a conducted agent (Super P 20 wt%, Power Source Battery Co., Taiyuan), and polyvinylidene fluoride (PVDF 10 wt%, Shanghai East Fluorine Chemical Technology Co., Ltd.) as a binder dissolved in *N*-methyl-2-pyrrolidinone (NMP, Shanghai Chemical Reagent Co., Ltd.) solution. Then the slurries with a thickness of 100 μm were coated onto copper foil substrates. And the sheets were dried at 120 °C under vacuum conditions for 24 h. After being cooled naturally to the ambient temperature, the copper foils with coated slurries were cut into φ14 mm disks, indicating 0.5 mg cm^{-2} of Si NSs@C nanopowder was loaded

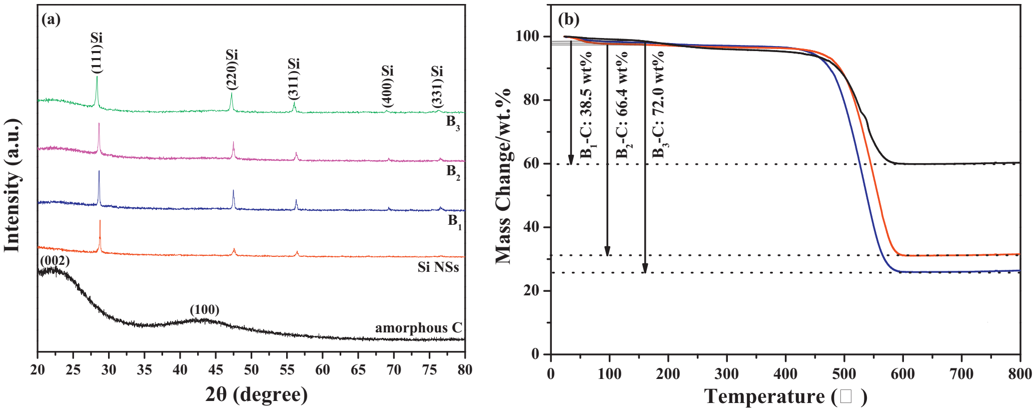

Fig. 1. (a) XRD patterns of phenolic resin-based carbon, as-prepared Si NSs and Si NSs@C nanocomposite powder with different carbon contents, (b) TGA curves of Si NSs@C nanocomposite powder with different carbon contents in an air atmosphere.

onto the Cu foil. For the sake of contrast, Si NSs electrode was prepared using the same method.

Cyclic voltammetry (CV) measurements were performed on an electrochemical workstation (CHI660D) at a scanning rate of 0.1 mV s^{-1} in the potential range of 0.01–2 V. The electrochemical impedance spectroscopy (EIS) was also carried out using the electrochemical workstation at a 5 mV amplitude signal in the frequency range from 100 KHz to 0.01 Hz. The galvanostatic charge/discharge performances at various current densities were measured by Land CT2001A in a voltage window of 0.01–2.00 V (vs. Li/Li^+).

3. Results and discussion

3.1. Phases, carbon contents and microstructures of Si NSs@C nanocomposites

X-ray diffraction (XRD) patterns of phenolic resin-based carbon, as-prepared Si NSs and Si NSs@C nanocomposite powder with different carbon contents (samples B_1, B_2 and B_3) are presented in Fig. 1a. Diffraction peaks of Si NSs located at $2\theta = 28.4°$, 47.2°, 56.1°, 69.1° and 76.3° are related to the (111), (220), (311), (400) and (331) crystal planes of Si with a cubic structure (JCPDS No. 27–1402). As for pyrolyzed phenolic resin-based carbon, two broad diffraction peaks can be observed at $2\theta = 23°$ and 43°, which are assigned to the (002) and (100) planes of carbon species (JCPDS No. 12–0212), indicating the relatively low graphitization degree and amorphous structure [33]. Compared with diffraction peak of graphite at 26°, the peak of (002) planes shifts to 23°, resulting from the decreased intermolecular forces and the increased interlayer spacing of $d_{(002)}$ [34,40]. For as-prepared Si NSs@C nanocomposites, the peak position and shape of crystal Si maintained unchanged and a broad hump at $2\theta = 23°$ could also be observed, indicating the introduction of carbon did not change the crystal structure of Si and no impurity phases were formed in the pyrolysis process. Fig. 1b shows the TGA curves of Si NSs@C nanocomposites. Residual carbon contents in samples B_1, B_2 and B_3 after phenolic resin were pyrolyzed were separately 38.5 wt%, 66.4 wt% and 72.0 wt%.

In Fig. 2, the bright field TEM and high-resolution TEM images show the microstructures and morphologies of Si NSs and Si NSs@C nanocomposites with different carbon contents. It is found that the Si NSs exhibit similar morphology and uniform size of 31 nm (Fig. 2a) with a thin thickness of 2.4 nm characterized via atomic force microscope (AFM) in our previous paper [15]. Each piece of Si NSs has distinct edges and corners, showing a more pure and continuous flake-like structure. The lattice spacing of Si NSs measured in Fig. 2a′ is 0.31 nm, corresponding to the (111) crystal plane of Si. The result of selected area electron diffraction (SAED) in our previous paper [15] can also reveal the crystalline state of Si NSs. As for samples B_1, B_2 and B_3, Si NSs were coated entirely by phenolic resin-based amorphous carbon, forming a stable structure as shown in Fig. 2(b, c and d). With increased amount of phenolic resin in the preparation process, the amorphous carbon layer became thicker and Si NSs were wrapped deeper. Fig. 2(b′, c′ and d′) shows the high-resolution TEM images of the three samples. And obvious lattice fringes can be seen, which is the same as that in Fig. 2a′. This verifies the existence of crystal Si phase. There is no obvious lattice fringe of the coating layer, which also proves that the pyrolyzed phenolic resin has disordered structures with low degree of graphitization.

Raman spectroscopy is carried out to examine the degree of graphitization and the imperfections in the obtained Si NSs@C nanocomposites with different carbon contents (Fig. 3). Three intensive peaks are displayed in all of the samples, denoted as Si-Si band (501 cm^{-1}), D-band (1325 cm^{-1}) and G-band (1589 cm^{-1}), respectively. The G-band is characteristic of graphitic sheets, corresponding to a well-defined sp^2 carbon-type structure, whereas the D-band can be attributed to the presence of defects within the hexagonal graphitic structure [35]. They provide extra evidence of the existence of carbon with low degree of graphitization in the composites. The intensity ratio of the D to G band (I_D/I_G) is generally employed to evaluate the extent of structural disorder for the carbon materials [36]. In samples of B_1, B_2 and B_3, the values of I_D/I_G are separately 0.87, 0.93 and 0.90. The maximum I_D/I_G ratio indicates more defects and disorders exist in the carbon coated on Si NSs surface [37]. This is beneficial to improving the excellent electrical conductivity, reducing the volume variation and getting high coulombic efficiency. Furthermore, amorphous carbon coated on Si NSs surfaces could facilitate the formation of stable SEI films.

3.2. Electrochemical properties of Si NSs@C nanocomposite electrodes

3.2.1. The cyclic voltammograms

Cyclic voltammetry (CV) curves of Si NSs@C nanocomposite electrodes at a scanning rate of 0.1 mV s^{-1} over a voltage range of 0.01–2 V are presented in Fig. 4a-c. In the first cathodic sweeping curves, the irreversible reduction peaks (R_1) appearing at 1.78 V, 1.41 V and 1.47 V for samples B_1, B_2 and B_3 may be attributed to side reactions between the electrolyte and the electrode surfaces, which disappears in subsequent cycles. Other irreversible reduction peaks (R_2) at 0.66 V (sample B_1), 0.51 V (sample B_2) and 0.50 V (sample B_3) correspond to formation of solid electrolyte interface (SEI) caused by the decomposition reaction of electrolyte on the surface of active components, which also disappears in further cycles [38,39]. Moreover, for sample B_3, a tiny irreversible reduction peak appears at around 2.0 V which is also thought to be one of side reactions of the electrolyte decomposition

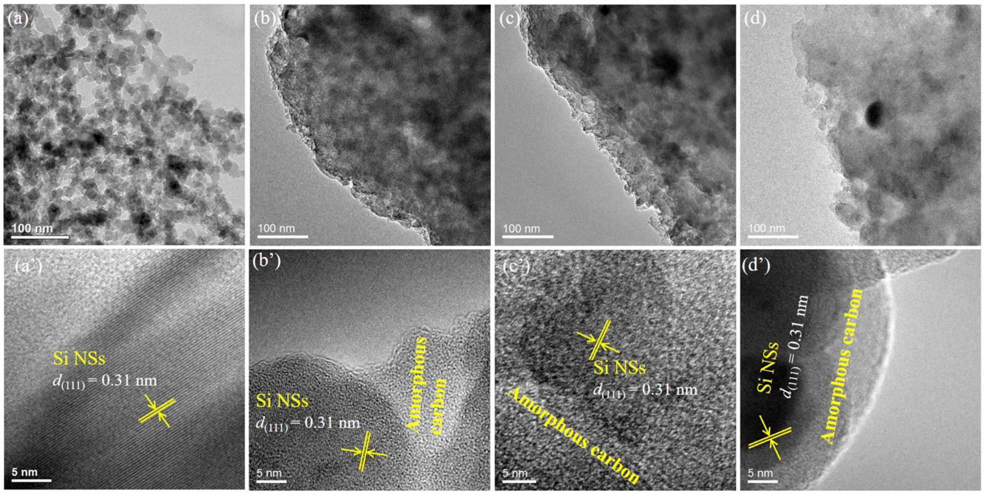

Fig. 2. TEM images of Si NSs (a, a′) and Si NSs@C nanocomposites with different carbon contents, including sample B_1 (b, b′), sample B_2 (c, c′), and sample B_3 (d, d′).

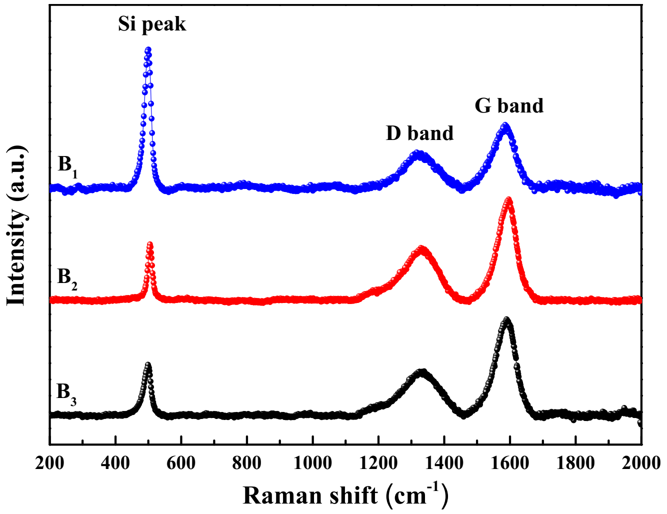

Fig. 3. Raman spectra of Si NSs@C nanocomposites with different carbon contents.

[40]. In addition to the reduction peaks of R_1 and R_2, dominating lithiation reaction with Si NSs takes place at about 0.01 V [41]. And the crystal structure of Si NSs will be destroyed and transformed into amorphous state (Li_xSi).

From the first anodic scanning, the two oxide peaks (O_1 and O_2) located at 0.33 V and 0.49 V in Fig. 4a are ascribed to the delithiation process from amorphous Li_xSi at low and high potentials. Relatively poor electrical contact and inhomogeneous lithiation formed in this sample due to the weaker intercalation kinetics and the minimum carbon content can rarely form an effective conductive framework. Therefore, the delithiation process cannot be completed at low potential. However, for samples B_2 and B_3, there is only one oxide peak at the potential of 0.42 V (Fig. 4b) and 0.44 V (Fig. 4c). Higher carbon contents improve the conductivity of electrodes and increase the electrical contact between active units, which is beneficial to the delithiation process. Besides the oxidation peaks of O_1 and O_2, another hump at around 1.1 V generated in all of three samples corresponds to the oxidation of electrolyte [42]. The carbon derived from phenolic resin by pyrolyzing shows no exact peaks in discharge-charge processes. It also suggests that the capacity of Si NSs@C nanocomposite electrodes mainly be governed by Si NSs.

In the second and third cycles, Si would hold its amorphous state to further react with Li^+ ions. Because this reaction is kinetically slow and the diffusion of Li^+ ions is dominant at a low rate, so no apparent lithiation peak can be found in the cathodic sweeping [43]. For oxidation peaks, the potential positions of three samples are consistent with that of the first cycle, but the peak current signals increase with cycling numbers, indicating the successive activation process has happened in electrodes [44]. In the first cycle, Si NSs wrapped deeply in the carbon matrix hardly participate in the lithiation process. As the cycles proceeding, the structure of Si NSs changes a lot with the volume expansion and contraction, and part of Si NSs gradually exposes and participates in the lithiation/delithiation reactions.

3.2.2. Cycling performance and rate capability

Fig. 5a-b provide the discharge/charge curves of Si NSs@C nanocomposite electrodes for the initial two cycles, at a current density of 100 mA g^{-1} over a potential range of 0.01–2 V. For samples B_1, B_2 and B_3, the first discharge specific capacities are separately 2990 mAh g^{-1}, 1846 mAh g^{-1} and 1227 mAh g^{-1}, giving a low initial Coulombic efficiency of 44%, 39% and 36%, respectively, which still needs to be improved in the future. Different specific capacity values are caused by induced diverse carbon contents. Sample B_1 in Fig. 5a shows further that there are two small sloping lithiation plateaus at the potential of ca. 1.3 V and 0.7 V, assigning to the side reactions between electrolyte and electrode surfaces as well as the formation of SEI film. In this process, part of Li^+ ions is consumed, resulting in the irreversible specific capacity loss. Thereafter, a continuously decreased plateau at the cut-off voltage of 0.01 V is ascribed to the lithiation of crystal Si. In the following 2nd discharge curve (Fig. 5b), the platforms at ca. 1.3 V and 0.7 V disappear, the inclined asymptote close to the bottom confirms the lithiation reaction between Li^+ ions and amorphous Si. In the initial two charge curves, the platforms in the similar potential range of 0.3–0.5 V are attributed to the delithiation from Li-Si alloys. For samples B_2 and B_3, semblable cycle curves are shown in Fig. 5a-b. Another point, the Coulombic efficiencies of samples B_1, B_2 and B_3 increase to 80%, 87% and 81% in the second cycle respectively, indicating that the presence of carbon buffers the continuous volume expansion of Si NSs, prevents the generation of new surfaces to regenerate SEI films, and facilitates the transfer of electrons and Li^+ ions.

To investigate and compare the electrochemical performances of Si NSs and Si NSs@C nanocomposites as anodes of LIBs, Fig. 6a shows the rate capabilities at different current densities ranging from 0.1 A g^{-1} to 2 A g^{-1}, in a voltage window of 0.01–2 V. For sample B_1, the capacity is much higher at a lower current density of 0.1 A g^{-1}, but decreases quickly as the current density increases to 2 A g^{-1}, i.e. from 1386 mAh g^{-1} to 450 mAh g^{-1}, resulting from lower carbon content. This cannot constitute effective electrical connection between Si NSs

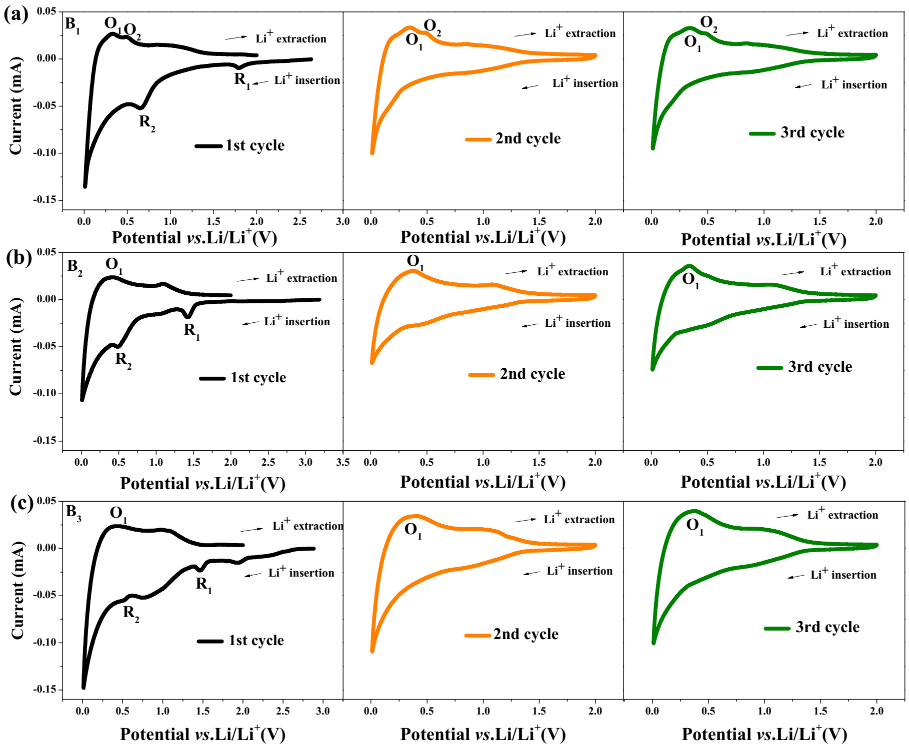

Fig. 4. The cyclic voltammogram curves of 1st, 2nd and 3rd cycles of Si NSs@C nanocomposite electrodes with different carbon contents, for (a) sample B_1, (b) sample B_2 and (c) sample B_3, scanned at a rate of 0.1 mV s^{-1} over a potential range of 0.01–2.00 V.

units. For sample B_2, as the current density increases from 0.1 A g^{-1} to 2 A g^{-1}, the cell can deliver more stable discharge specific capacities of 866 mAh g^{-1} to 558 mAh g^{-1}. The cell of sample B_3 behaves lower capacities of 337 mAh g^{-1} and 91 mAh g^{-1} at the current densities of 0.1 A g^{-1} and 2 A g^{-1}. When the current density returns back to 0.1 A g^{-1}, the battery capacities of samples B_1, B_2 and B_3 can recover to 1125 mAh g^{-1}, 891 mAh g^{-1} and 576 mAh g^{-1}. But for Si NSs electrode, the capacity declines quickly to 40 mAh $^{-1}$ after 20 cycles, which is attributed to the severe pulverization and structural collapse of electrode. Quite steady and satisfactory rate capabilities of Si NSs@C nanocomposite electrodes are ascribed to the stable structure and strong electrical contact between Si NSs and carbon coating layers in the nanocomposite microstructure. This provided a rapid transport passageway for electrons and Li$^+$ ions. Among the three electrodes, sample B_2 is the best in response to the high current density and the resilient ability, due to the balanced contents of active Si NSs and conductive carbon.

The cycling performances of Si NSs@C nanocomposite electrodes as well as the Coulombic efficiencies at 0.1 A g^{-1} between 0.01 and 2 V tested continuously after rate capabilities are shown in Fig. 6b. It has been reported many times that the specific capacity of bare Si electrode would drop rapidly within several cycles. In the present paper, as comparison, the capacity of Si NSs electrode within 100 cycles is also shown in Fig. 6b. It declines quickly to 180 mAh g^{-1} after 30 cycles, resulting from the huge volume variation, structural fracture, loss of electrical contact during lithiation/delithiation processes and the parasitic issues, such as repeated formation of thick SEI layer. But for Si NSs@C nanocomposite electrodes, significantly improved specific capacities of 803 mAh g^{-1} (sample B_1), 822 mAh g^{-1} (sample B_2) and 603 mAh g^{-1} (sample B_3) could be maintained after 200 cycles with the enhanced Coulombic efficiencies of 99.57%, 99.84% and 99.22%, respectively. The improved capacities and cycle stability are influenced by the following factors. The carbon coating layer can serve as an electron transport channel and a structural scaffold, keeping an intimate and robust electrical contact between Si NSs regardless of the repeated changes in large volume. Amorphous carbon can also protect

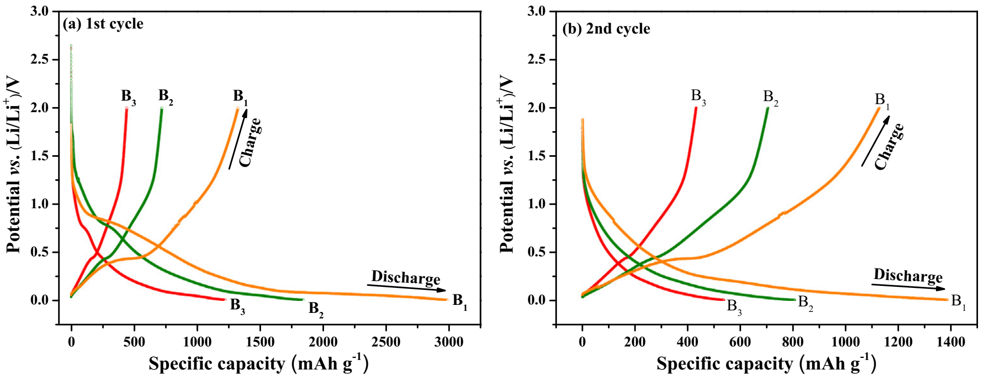

Fig. 5. The galvanostatic discharge/charge profiles for 1st (a) and 2nd (b) cycles of Si NSs@C nanocomposite electrodes with different carbon contents, at a current density of 100 mA g^{-1} over a potential range of 0.01–2.00 V.

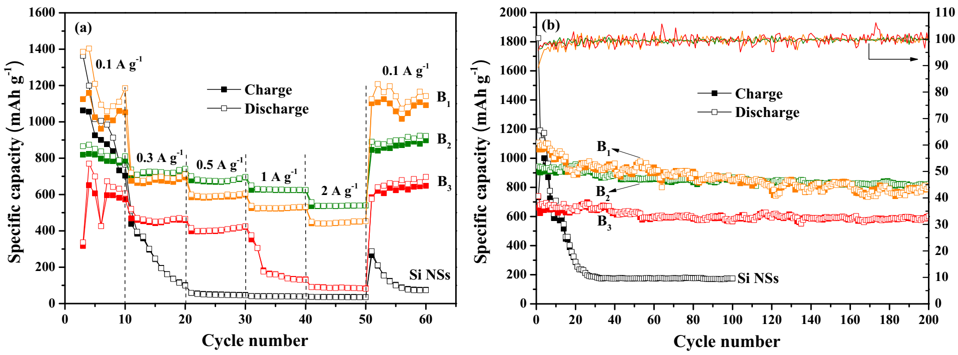

Fig. 6. (a) Rate capabilities of Si NSs and Si NSs@C nanocomposite electrodes at current densities from 0.1 A g^{-1} to 2 A g^{-1} in a voltage window of 0.01–2 V. (b) Cycling performances of Si NSs, Si NSs@C nanocomposite electrodes at a current density of 100 mA g^{-1} between 0.01 and 2 V, and Coulombic efficiencies of Si NSs@C nanocomposite electrodes within 200 cycles.

Si NSs from direct exposure to electrolyte, guaranteeing the stable formation of SEI film, and thus improving the cycle stability. Furthermore, it can be seen from Fig. 6b that the Coulombic efficiencies of Si NSs@C nanocomposite electrodes are unstable with cycles. It is thought, in spite of the derived carbon matrix with unique texture, that the framework of phenolic resin is still maintained [45]. And the Si NSs inside are difficult to completely participate in the lithiation/delithiation process. As the reaction proceeds, the framework structure will be destroyed and the Si NSs inside will gradually expose to react with Li^+ ions, showing the electrochemical activity. In other words, the Si NSs@C nanocomposite electrode owns an activation process during cycling, so the discharge/charge specific capacities will not keep stable until Si NSs are fully involved in the reaction. It is remarkable that sample B_2 has the most stable reversible capacity with a minimum fluctuation in Coulombic efficiency. And the capacity of sample B_1 shows decreased tendency all the time. For sample B_3, the capacity is the lowest on account of the presence of much carbon. Testing results also declare that the content of phenolic resin-based amorphous carbon should be under control. Thus, more carbon will form thicker buffer layers. Si NSs coated deep inside have no chance to participate in the reaction, leading to low specific capacity. Less carbon is unable to sustain the volume variation and stable conductive framework upon the lithiation/delithiation process, resulting in the instability of electrochemical cycling.

3.2.3. Electrochemical impedance spectra

It is clear that the Si NSs@C nanocomposite electrode with the carbon content of 66.4 wt% (sample B_2) shows the best stable electrochemical performance in this paper, thus we have made a further analysis about electric property compared with Si NSs on it. The electrochemical impedance spectroscopy (EIS) for the initial and cycled states of Si NSs and sample B_2 electrodes are analyzed by Nyquist plots as presented in Fig. 7a-b. The experimental results, fitting data and the corresponding equivalent circuits are also displayed together. It is indicated in Fig. 7a that the impedance spectra of initial electrodes are composed of a bigger semicircle at high frequency and an inclined line at low frequency range. Among them, the semicircle represents the resistance caused by the charge transport inside the active phases, while the inclined line implies Warburg impedance, i.e. the solid-state diffusion resistance of Li^+ ions in the active material. After three cycles, both impedance spectra consist of two depressed semicircles at high/medium frequency regions and one inclined line at low frequency. The first semicircle at high frequency denotes the migration resistance of Li^+ ions in SEI films. The second semicircle at medium frequency means the charge transport resistance, which is similar to the case of initial electrode. And the inclined line at low frequency represents Warburg impedance.

These impedances are numerically simulated by the analog circuits for the initial case and cycled ones, as shown in the insets of Fig. 7a-b, respectively. Here, R_1 is the contact resistance at the interface between electrolyte and electrode. R_2 is the transfer resistance of Li^+ ions. R_3 is the charge transfer resistance in electrolyte. CPE_{dl} is the double layers capacitance between the electrode and the electrolyte. CPE_s is the SEI film capacitance. And W is the Warburg impedance of Si NSs and sample B_2 electrodes. Faradic current density (I_F) and the diffusion coefficient (D_0) of Li^+ ions are calculated by the following Eqs. (1)–(3) [46]. And the results are listed in Table 1.

$$Z' = R_1 + R_{ct} + \sigma_w \omega^{-0.5} \tag{1}$$

$$I_F = RT/nAFR_2 \tag{2}$$

$$D_0 = 0.5(RT/AF^2\sigma_w C)^2 \tag{3}$$

where R_{ct} is the transfer resistance of Li^+ ions. R is the gas constant (8.314 J mol^{-1} K^{-1}). F is the Faraday constant (9.6485×10^4 C mol^{-1}). T is the room temperature (298 K). A is the contact area between the electrolyte and the electrode. σ_w is the Warburg coefficient. ω is the angular frequency in the low frequency region. C is the molar concentration of Li^+ ions. And n is the number of electrons transferred in every molecule during the intercalation.

From Table 1, the R_1 value of Si NSs electrode in the initial cycle is

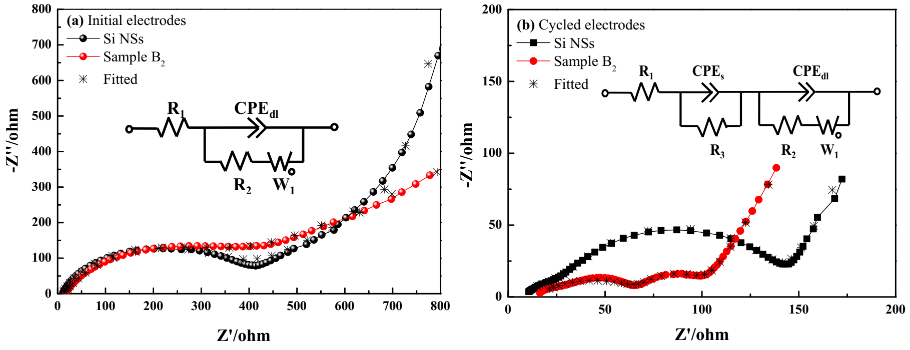

Fig. 7. Nyquist plots and fitting curves for the electrodes of Si NSs and sample B_2 (a) in the initial state, (b) after three cycles. The insets are equivalent circuit models for EIS analysis on each of electrode's states.

Table 1
Equivalent circuit parameters of Si NSs and sample B_2 electrodes in the initial state and after three cycles.

Samples	Initial state				After three cycles			
	$R_1/(\Omega\Omega)$	$R_{ct}/(\Omega\Omega)$	$D_0/(m^2 \cdot s^{-1})$	$I_F/(mA \cdot cm^{-2})$	$R_1/(\Omega\Omega)$	$R_{ct}/(\Omega\Omega)$	$D_0/(m^2 \cdot s^{-1})$	$I_F/(mA \cdot cm^{-2})$
Si NSs	9.6	370.3	$4.98 * 10^{-16}$	$4.51 * 10^{-2}$	2.6	138.8	$6.90 * 10^{-16}$	$1.96 * 10^{-1}$
B_2	14.3	338.8	$5.90 * 10^{-17}$	$4.93 * 10^{-2}$	13.3	91.9	$5.34 * 10^{-14}$	$5.24 * 10^{-1}$

smaller than that of sample B_2 electrode, which is attributed to different degrees of electrolyte infiltration in electrodes [47]. But the reverse results can be found for Li^+ ion transfer resistance (R_{ct}). This declares that the Si NSs coated in the carbon layer is beneficial to the fast transport of Li^+ ions and electrons. After three cycles, the values of R_{ct} separately decrease from 370.3 Ω to 138.8 Ω and 338.8 Ω to 91.9 Ω for Si NSs and sample B_2 electrodes, meaning a favorable electrical contact is formed inside of the nanocomposite, which improves the transferability of electrons and Li^+ ions. The existence of carbon is also helpful to form a stable SEI film and construct a stable conductive network [48,49]. Furthermore, the increase of Faradic current density (I_F) and diffusion coefficient (D_0) values after three cycles indicates that the highly effective redox reactions have been allowed to occur in both electrodes due to the enhanced reaction kinetics [50]. Compared with Si NSs electrode, the electrochemical parameters of sample B_2 electrode improve a lot. Therefore, highlighting the existence of carbon layer is conducive to the enhancement of electrochemical performance.

4. Conclusion

Two-dimensional Si NSs were successfully synthesized by DC arc-discharge plasma, and the Si NSs@C nanocomposites with different carbon contents were subsequently fabricated through the high-temperature pyrolysis of phenolic resin. Si NSs are about 31 nm in mean size and near 2.4 nm in sheet thickness. Those are coated by the phenolic resin-derived amorphous carbon to form the nanocomposite with cladding structure. Comparing with bare Si NSs electrode, the Si NSs@C nanocomposite electrodes show enhanced electrochemical performance due to their unique structure. The carbon coating can provide an intimate and robust electrical contact among the Si NSs phases, and hence can offer a rapid transport passageway for electrons and Li^+ ions. It can also protect Si NSs from direct exposure to the electrolyte, guaranteeing the formation of stable SEI films. Moreover, the cycling stability and the capacity retention are able to be controlled by the different amounts of carbon introduced. For the Si NSs@C nanocomposite electrode with the carbon content of 66.4 wt%, it delivers a stable discharge specific capacity of 822 mAh g^{-1} at a current density of 100 mA g^{-1} after 200 cycles. It is believed that the Si NSs@C nanocomposites fabricated by the facile arc-discharge plasma and high-temperature pyrolysis methods are designable and beneficial in the anode materials of LIBs with higher energy/power densities.

Acknowledgements

This work was supported by the National Natural Science Foundation of China (Nos. 51331006 and 51271044).

References

[1] M. Hu, X.L. Pang, Z. Zhou, Recent progress in high-voltage lithium ion batteries, J. Power Sources 237 (2013) 229–242.
[2] F. Zheng, Y. Yang, Q. Chen, High lithium anodic performance of highly nitrogen-doped porous carbon prepared from a metal-organic framework, Nat. Commun. 5 (2014) 5261–6261.
[3] B. Scrosati, J. Garche, Lithium batteries: status, prospects and future, J. Power Sources 195 (2010) 2419–2430.
[4] H.D. Chen, Z.L. Wang, X.H. Hou, L.J. Fu, S.F. Wang, X.Q. Hu, H.Q. Qin, Y.P. Wu, Q. Ru, X. Liu, S.J. Hu, Mass-producible method for preparation of a carbon-coated graphite@plasma nano-silicon@carbon composite with enhanced performance as lithium ion battery anode, Electrochim. Acta 249 (2017) 113–121.
[5] K.F. Chen, H. Yang, F. Liang, D.F. Xue, Microwave irradiation assisted combustion towards modified graphite as Lithium ion battery anode, ACS Appl. Mater. Interfaces 10 (2018) 909–914.
[6] R.Z. Liu, Y. Zhang, Z.J. Ning, and Y.X. Xu, A catalytic microwave process for superfast preparation of high-quality reduced graphene oxide, Angew. Chem. Int. Ed. 56 (2017) 56 15677–15682.
[7] O. Fromm, A. Heckmann, U. Rodehorst, J. Frerichs, D. Becker, M. Winter, T. Placke, Carbons from biomass precursors as anode materials for lithium ion batteries: new insights into carboni zation and graphitization behavior and into their correlation to electrochemical perf romance, Carbon 128 (2018) 147–163.
[8] S.Q. Wang, N.Q. Zhao, C.S. Shi, E.Z. Liu, C.N. He, F. He, L.Y. Ma, In-situ grown CNTs modified SiO_2/C composites as anode with improved cycling stability and rate capability for lithium storage, Appl. Surf. Sci. 433 (2018) 428–436.
[9] I.H. Son, J.H. Park, S. Kwon, J.W. Choi, M.H. Rümmeli, Graphene coating of silicon nanoparticles with CO_2-enhanced chemical vapor deposition, Small 12 (2016) 658–667.
[10] J.G. Qin, M.Q. Wu, T.T. Feng, C. Chen, C.Y. Tu, X.H. Li, C. Duan, D.W. Xia, D.X. Wang, High rate capability and long cycling life of graphene-coated silicon composite anodes for lithium ion batteries, Electrochim. Acta 256 (2017) 259–266.
[11] G.M. Liang, X.Y. Qin, J.S. Zou, L.Y. Luo, Y.Z. Wang, M.Y. Wu, H. Zhu, G.H. Chen, F.Y. Kang, B.H. Li, Electrosprayed silicon-embedded porous carbon microspheres as lithium-ion battery anodes with exceptional rate capacities, Carbon 127 (2018) 424–431.
[12] S. Cho, H.Y. Jang, I. Jung, L.C. Liu, S. Park, Synthesis of embossing Si nanomesh and its application as an anode for lithium ion batteries, J. Power Sources 362 (2017) 270–277.
[13] S.W. Lee, M.T. McDowell, L.A. Berla, W.D. Nix, Y. Cui, Fracture of crystalline silicon nanopillars during electrochemical lithium insertion, PNAS 109 (2012) 4080–4085.
[14] Y. Yao, M.T. McDowell, I. Ryu, H. Wu, N. Liu, L.B. Hu, W.D. Nix, Y. Cui, Interconnected silicon hollow nanospheres for lithium-ion battery anodes with long cycle life, Nano Lett. 11 (2011) 2949–2954.
[15] X.H. Yu, F.H. Xue, H. Huang, C.J. Liu, J.Y. Yu, Y.J. Sun, X.L. Dong, G.Z. Cao, Y.G. Jung, Synthesis and electrochemical properties of silicon nanosheets by DC arc discharge for lithium-ion batteries, Nanoscale 6 (2014) 6860–6865.
[16] J.T. Wang, H. Wang, B.C. Zhang, Y. Wang, S.G. Lu, X.H. Zhang, A stable flexible silicon nanowire array as anode for high-performance lithium-ion batteries, Electrochim. Acta 176 (2015) 321–326.
[17] B.D. Polat, O.L. Eryilmaz, O. Keles, A. Erdemir, K. Amine, Compositionally graded Si-Cu thin film anode by magnetron sputtering for lithium ion battery, Thin Solid Films 596 (2015) 190–197.
[18] Y.Y. Kim, J.H. Lee, H.J. Kim, Nanoporous silicon flakes as anode active material for lithium-ion batteries, Phys. E. 85 (2017) 223–226.
[19] X.H. Zhang, X.Y. Qiu, D.B. Kong, L. Zhou, Z.H. Li, X.L. Li, L.J. Zhi, Silicene flowers: a dual stabilized silicon building block for high-performance lithium battery anodes, ACS Nano 11 (2017) 7476–7484.
[20] Z.L. Xu, K. Cao, S. Abouali, M.A. Garakani, J.Q. Huang, E.K. Heidari, H.T. Wang, J.K. Kim, Study of lithiation mechanisms of high performance carbon-coated Si anodes by in-situ microscopy, Energy Storage Mater. 3 (2016) 45–54.
[21] C.Y. Du, M. Chen, L. Wang, G.P. Yin, Covalently-functionalizing synthesis of Si@C core-shell nanocomposites as high-capacity anode materials for lithium-ion batteries, J. Mater. Chem. 21 (2011) 15692–15697.
[22] Y.H. Xu, G.P. Yin, Y.L. Ma, P.J. Zuo, X.Q. Cheng, Nanosized core/shell silicon@carbon anode material for lithium ion batteries with polyvinylidene fluoride as carbon source, J. Mater. Chem. 20 (2010) 3216–3220.
[23] K. Fu, L.G. Xue, O. Yildiz, S.L. Li, H. Lee, Y. Li, G.J. Xu, L. Zhou, P.D. Bradford, X.W. Zhang, Effect of CVD carbon coatings on Si@CNF composite as anode for lithium-ion batteries, Nano Energy 2 (2013) 976–986.
[24] H.W. Yue, Q. Li, D.Q. Liu, X.Y. Hou, S. Bai, S.M. Lin, D.Y. He, High-yield fabrication of graphene-wrapped silicon nanoparticles for self-support and binder-free anodes of lithium-ion batteries, J. Alloys Compd. 744 (2018) 243–251.
[25] H.Y. Cai, K. Han, H. Jiang, J.W. Wang, H. Liu, Self-standing silicon-carbon nanotube/graphene by a scalable in situ approach from low-cost Al-Si alloy powder for lithium ion batteries, J. Phys. Chem. Solids 109 (2017) 9–17.
[26] Z.L. Xu, B. Zhang, J.K. Kim, Electrospun carbon nanofiber anodes containing monodispersed Si nanoparticles and graphene oxide with exceptional high rate capacities, Nano Energy 6 (2014) 27–35.
[27] B.Y. Lee, T.Y. Liu, S.K. Kim, H. Chang, K. Eom, L.X. Xie, S. Chen, H.D. Jang, S.W. Lee, Submicron silicon encapsulated with graphene and carbon as a scalable anode for lithium-ion batteries, Carbon 119 (2017) 438–445.
[28] T. Shen, X.H. Xia, D. Xie, Z.J. Yao, Y. Zhong, J.Y. Zhan, D.H. Wang, J.B. Wu, X.L. Wang, J.P. Tu, Encapsulating silicon nanoparticles into mesoporous carbon forming pomegranate structured microspheres as a high-performance anode for lithium ion batteries, J. Mater. Chem. A 5 (2017) 11197–11203.

[29] J.Y. Yu, J. Gao, F.H. Xue, X.H. Yu, H.T. Yu, X.L. Dong, H. Huang, A. Ding, X. Quan, G.Z. Cao, Formation mechanism and optical characterization of polymorphic silicon nanostructures by DC arc-discharge, RSC Adv. 5 (2015) 68714–68721.

[30] Y. Badhe, K. Balasubramanian, Reticulated three-dimensional network ablative composites for heat shields in thermal protection systems, RSC Adv. 4 (2014) 43708–43719.

[31] Y. Chen, C. Hong, P. Chen, The effects of zirconium diboride particles on the ablation performance of carbon-phenolic composites under an oxyacetylene flame, RSC Adv. 3 (2013) 13734–13739.

[32] C.T. Lin, H.T. Lee, J.K. Chen, Preparation and properties of bisphenol-F based boron-phenolic resin/modified silicon nitride composites and their usage as binders for grinding wheels, Appl. Surf. Sci. 330 (2015) 1–9.

[33] C.F. Zhang, H.B. Wu, C.Z. Yuan, Z.P. Guo, X.W. (David) Lou, Confining sulfur in double-shelled hollow carbon spheres for lithium-sulfur batteries, Angew. Chem. Int. Ed. 124 (2012) 1–5.

[34] H.L. Wang, Z.Q. Shi, J. Jin, C.B. Chong, C.Y. Wang, Properties and sodium insertion behavior of phenolic resin-based hard carbon microspheres obtained by a hydrothermal method, Electroanal. Chem. 755 (2015) 87–91.

[35] S. Stankovich, D.A. Dikin, R.D. Piner, K.A. Kohlhaas, A. Kleinhammes, Y. Jia, Y. Wu, S.T. Nguyen, R.S. Ruoff, Synthesis of graphene-based nanosheets via chemical reduction of exfoliated graphite oxide, Carbon 45 (2007) 1558–1565.

[36] J. Ye, J. Zang, Z. Tian, M. Zheng, Q. Dong, Sulfur and nitrogen co-doped hollow carbon spheres for sodium-ion batteries with superior cyclic and rate performance, J. Mater. Chem. A 4 (2016) 13223–13227.

[37] S.N. Yang, G.R. Li, Q. Zhu, Q.M. Pan, Covalent binding of Si nanoparticles to graphene sheets and its influence on lithium storage properties of Si negative electrode, J. Mater. Chem. 22 (2012) 3420–3425.

[38] X.Y. Feng, Q. Shen, Y.C. Shi, J.X. Zhang, One-pot hydrothermal synthesis of core-shell structured $MnCO_3$@C as anode material for lithium-ion batteries with superior electrochemical performance, Electrochim. Acta 220 (2016) 391–397.

[39] Q.S. Xie, L. Lin, Y.T. Ma, D.Q. Zeng, J.R. Yang, J. Huang, L.S. Wang, D.L. Peng, Synthesis of ZnO-Cu-C yolk-shell hybrid microspheres with enhanced electrochemical properties for lithium ion battery anodes, Electrochim. Acta 226 (2017) 79–88.

[40] L.L. Wang, Y.G. Liu, C.B. Chong, J. Wang, Z.Q. Shi, J. Pan, Phenolic formaldehyde resin/graphene composites as lithium-ion batteries anode, Mater. Lett. 170 (2016) 217–220.

[41] L.M. Wei, Z.Y. Hou, H. Wei, Porous sandwiched graphene/silicon anodes for lithium storage, Electrochim. Acta 229 (2017) 445–451.

[42] D.B. Polat, O. Keles, K. Amine, Compositionally-graded silicon copper helical arrays as anodes for lithium-ion batteries, J. Power Sources 304 (2016) 273–281.

[43] B.D. Polat, O. Keles, Multi-layered Cu/Si nanorods and its use for lithium ion batteries, J. Alloys Compd. 622 (2015) 418–425.

[44] H.C. Shin, J.A. Corno, J.L. Gole, M. Liu, Porous silicon negative electrodes for rechargeable lithium batteries, J. Power Sources 139 (2005) 314–320.

[45] W. Luo, Y.X. Wang, S.L. Chou, Y.F. Xu, W. Li, B. Kong, S.X. Dou, H.K. Liu, J.P. Yang, Critical thickness of phenolic resin-based carbon interfacial layer for improving long cycling stability of silicon nanoparticle anodes, Nano Energy 27 (2016) 255–264.

[46] Y. Cui, X.L. Zhao, R.S. Guo, Improved electrochemical performance of $La_{0.7}Sr_{0.3}MnO_3$ and carbon co-coated $LiFePO_4$ synthesized by freeze-drying process, Electrochim. Acta 55 (2010) 922–926.

[47] H. Huang, S. Gao, A.M. Wu, K. Cheng, X.N. Li, X.X. Gao, J.J. Zhao, X.L. Dong, G.Z. Cao, Fe_3N constrained inside C nanocages as an anode for Li-ion batteries through post-synthesis nitridation, Nano Energy 31 (2017) 74–83.

[48] C.J. Liu, F.H. Xue, H. Huang, X.H. Yu, C.J. Xie, M.S. Shi, G.Z. Cao, Y.G. Jung, X.L. Dong, Preparation and electrochemical properties of Fe-Sn (C) nanocomposites as anode for lithium-ion batteries, Electrochim. Acta 129 (2014) 93–99.

[49] C.J. Liu, H. Huang, G.Z. Cao, F.H. Xue, R.A.P. Camacho, X.L. Dong, Enhanced electrochemical stability of Sn-carbon nanotube nanocapsules as lithium-ion battery anode, Electrochim. Acta 144 (2014) 376–382.

[50] S. Gao, H. Huang, A.M. Wu, J.Y. Yu, J. Gao, X.L. Dong, C.J. Liu, G.Z. Cao, Formation of Sn-M (M = Fe, Al, Ni) alloy nanoparticles by DC arc discharge and their electrochemical properties as anodes for Li-ion batteries, J. Solid State Chem. (2016) 127–135.